Organic Spacer Cation Strategies for High-Quality Layered Perovskite Thin Films

Sophie Laurent
Department of Endocrinology, University of Bordeaux, France

Keywords: Ruddlesden-Popper, layered perovskite, solar cell, light-emitting diode

Abstract

Ruddlesden–Popper perovskites (RPPs), consisting of alternating organic spacer layers and inorganic layers, have emerged as a promising alternative to three-dimensional perovskites for both photovoltaic and light-emitting applications. The organic spacer layers provide a wide range of new possibilities to tune the properties and even provide new functionalities for RPPs. However, the preparation of state-of-the-art RPPs requires organic ammonium halides as the starting materials, which need to be *ex situ* synthesized. This work presents a novel approach to prepare high-quality RPP films through in situ formation of organic spacer cations from amines. Compared with the control devices fabricated from organic ammonium halides, this new approach results in similar (and even better) device performance for both solar cells and light-emitting diodes (LEDs). High-quality RPP films are fabricated based on different types of amines, demonstrating the universality of the approach. This approach not only represents a new pathway to fabricate efficient devices based on RPPs, but also provides an effective method to screen new organic spacers with further improved performance.

Halide perovskites with three-dimensional (3D) crystal structures have attracted intense research interest due to their great success in high-performance optoelectronic devices.[1-5] A power conversion efficiency (PCE) of 25.2% and an external quantum efficiency (EQE) over 20% have been realized for perovskite solar cells and light-emitting diodes (LEDs), respectively.[6-8] In spite of these significant advances, 3D perovskites suffer from intrinsic instability over moisture, light and heat.[9,10]

Recently, Ruddlesden–Popper perovskites (RPPs) with a formula of $(RNH_3)_2A_{n-}$

$_1M_nX_{3n+1}$ have been explored as a promising alternative to their 3D counterparts.[11,12] For a typical RPP, cations A^+, M^{2+} and halide anions X^- form octahedral perovskite frameworks, and RNH_3^+ cations are excluded from the 3D perovskite structure due to large ionic radius and act as organic spacers between the perovskite planes, resulting in a structure of alternately stacked organic and perovskite layers. Compared to their 3D counterparts, RPPs show enhanced ambient stability in solar cells,[13,14] although the device efficiency is sacrificed to some extent. In addition, they also show compact and pinhole-free film morphology upon simple processing and remarkably enhanced photoluminescence quantum yields (PLQY) to enable high-efficiency LEDs.[15,16] These advantages make RPPs very attractive in both solar cells and LEDs.[12,17,18] More importantly, the organic spacer cations (RNH_3^+) provide enormous tunability by molecular design, such as changes of the alkyl chain length, insertion of π-conjugated segments and introduction of functional groups, which could in turn tune optoelectronic properties of RPPs.[19-21] The versatility of RNH_3^+ offers great opportunities for RPPs to achieve new properties for various applications.[22]

However, the starting materials for the RNH_3^+ of RPPs have been limited to organic ammonium halides (RNH_3X, X = Cl, Br, I), while the commercially available materials are mostly organic amines (RNH_2).[15,23,24] Chemical synthesis of RNH_3X is usually required before they are applied in perovskite precursor solutions, raising barriers for the development of new RPPs.[15,25]

In this work, we develop a novel approach for convenient deposition of RPP films through directly using RNH_2 to in situ form RNH_3^+, thus avoiding the extra chemical synthesis processes of RNH_3X. We choose the commonly employed $(PEA)_2(MA)_3Pb_4I_{13}$ (PEA = $C_6H_5(CH_2)_2NH_3^+$, MA = $CH_3NH_3^+$) RPP as an example, and replace PEAI in the control precursor with phenethylamine ($PENH_2$) and HI, NH_4I or MAI, respectively, to prepare three new precursor solutions. The resulting RPP films all show high qualities as evidenced by a range of characterizations and excellent device performance, indicating the effectiveness of our

new approach for RPP films. Remarkably, we achieve a high PCE of 14.3% with a high open-circuit voltage (V_{OC}) of 1.22 V for MAI-based RPP (n = 4) solar cells, which is among the highest reported values for RPP devices.[26] Moreover, different types of RNH_2 with aliphatic, electron-donating aryl, aryl ether, heterocyclic aromatic and polycyclic aromatic building blocks are investigated to demonstrate the universality of our method. High-quality RPP films are realized based on these RNH_2, enabling efficient RPP solar cells and LEDs. Impressively, an efficient deep red LED is achieved with a peak EQE of 6.0%, which is among the best red RPP LEDs.[27] Our finding provides a novel and efficient approach to prepare high-quality RPP films from commercially available RNH_2, which will help to spur the development of RPPs for various optoelectronic applications.

Our previous work has successfully demonstrated high-quality $(PEA)_2(MA)_3Pb_4I_{13}$ RPP films with vertically oriented perovskite frameworks and type-II band alignment, achieving a high PCE of 12.1% for solar cells.[28] The precursor solution in that case was to dissolve PbI_2, MAI, and PEAI (4:3:2 molar ratio) in anhydrous dimethylformamide (DMF) with dimethylsulfoxide (DMSO) and MACl additives, and was used as a control in this study. As described in the Experimental Section, our method for three new precursor solutions is to use $PENH_2$ together with HI, NH_4I and MAI, respectively, to replace PEAI while keeping all other components the same. It is assumed that in situ formation of PEAI could happen via the following three chemical equations:

$$PENH_2 + HI \rightarrow PEAI \quad (1)$$

$$PENH_2 + NH_4I \rightarrow PEAI + NH_3 \uparrow \quad (2)$$

$$PENH_2 + MAI \rightarrow PEAI + CH_3NH_2 \uparrow \quad (3)$$

In order to demonstrate that the above reactions can happen in aprotic DMF solvent, we first prepared three solutions by dissolving $PENH_2$ with equimolar HI, NH_4I and MAI, respectively, in DMF solvent. Three samples were prepared by spin-coating the solutions on glass substrates, followed by annealing at 100 °C for 5 min to remove the residual solvents in

a N_2-filled glovebox (O_2 and H_2O < 1 ppm). X-ray diffraction (XRD) measurements were conducted for the samples as well as purchased PEAI, NH_4I and MAI. As shown in **Figure 1**a, the XRD patterns of the three samples all show strong diffraction peaks at 4.6°, 9.3°, 18.6°, 23.3° and 28.0°, which are fully consistent with those of the purchased PEAI, confirming the formation of PEAI via Equation 1-3. In addition, from the XRD patterns (Figure S1, Supporting Information), we observe no residual NH_4I or MAI in the as-formed PEAI, suggesting almost complete transformation of the starting materials.

To further understand whether the reactions occur in solution or during film preparation, we first investigated the solution of $PENH_2$ with MAI by ^1H Nuclear Magnetic Resonance (NMR) spectroscopy. We observe no signal assigned to PEAI from the $PENH_2$ + MAI solution (Figure S2, Supporting Information), suggesting that the reaction does not start in solution. Then, we prepared film samples from three solutions dissolving $PENH_2$ with equimolar HI, NH_4I and MAI, respectively, in DMF solvent, which were annealed at 100 °C for different time. We measured the XRD patterns of these samples and observed strong diffraction peaks assigned to PEAI for the films even without annealing (Figure S3, Supporting Information). In addition, the films annealed for 1 min show stronger diffraction peaks, whereas longer-time annealing does not make any difference. These results indicate that PEAI in all the three reactions is mostly formed during processing with the evaporation of solvents. Equation 1 is a well-known reaction between Lewis acid (HI) and Lewis base ($PENH_2$), easily resulting in the product PEAI. Equation 2 and 3 are displacement reactions. Since the basicity of $PENH_2$, NH_3 and CH_3NH_2 are almost the same,[29,30] the driving force of the two reactions could be the removal of NH_3 and CH_3NH_2 gases due to the lower boiling points of NH_3 and CH_3NH_2 compared to $PENH_2$.

To confirm that our method could work for RPP films, we prepared $(PEA)_2PbI_4$ (n = 1) and $(PEA)_2MAPb_2I_7$ (n = 2) RPP precursor solutions in pure DMF by our method (See Experimental Section for details), which was used to fabricate RPP films on glass substrates in the glovebox. As shown in Figure S4 in Supporting Information, the resulting RPP films show

similar XRD and absorption characteristics compared to the control samples, suggesting that our method is applicable to fabricate RPP films.

In order to demonstrate efficient RPP solar cells by our method, we prepared larger-*n* RPP $(PEA)_2(MA)_3Pb_4I_{13}$ films by this novel approach (See Experimental Section for details). The XRD patterns of these films show very similar features with strong (110) and (220) diffraction peaks and narrow full-width at half-maximum (FWHM) of the (110) plane (Figure 1b), indicating highly preferred orientation and high crystallinity of the resulting films. Interestingly, the film from the MAI-based precursor shows the smallest value of FWHM (0.09°), which is still within the instrument resolution (0.07°), obtained from a calibration standard (LaB_6 specimen, Figure S5, Supporting Information). Such a small FWHM value suggests that it has better crystallinity than the control film from the PEAI-based precursor.[31,32] Figure 1c shows the UV–vis absorption spectra for the films. Similar absorption spectra with absorption onsets at ≈750 nm and several excitonic absorption peaks at higher energy can be observed, providing evidence that these films are a mixture of multiple RPP phases with different *n* values.[32,33] One may consider that the introduction of amines RNH_2 can also lead to the formation of RPPs. However, as shown in Figure S6 in Supporting Information, replacing PEAI in the precursor with $PENH_2$ on its own resulted in a completely different film by characterizations of absorption and XRD. It can be explained by the fact that $PENH_2$ consumed the MAI that is supposed to form the perovskite frameworks with PbI_2, leading to more RPP phases with smaller *n* values. This result indicates that it is necessary to use ammonium cations RNH_3^+ to form RPPs with desirable *n* values.

Steady-state photoluminescence (PL) spectra of the RPP films were obtained from both front excitation and back excitation (Figure S7, Supporting Information), which show a dominant emission peak at ≈755 nm (from large-*n* RPP phases). The spectra under back excitation show weak additional peaks at short wavelengths (from small-*n* RPP phases), indicating that the small-*n* RPP phases are located at the bottom of the films, which is consistent

with previous reports of RPP films.[28,32,33] In Figure 1d, we compare transient PL decay curves of the RPP films deposited on quartz substrates. All the curves were fitted using a bi-exponential function with the relevant parameters listed in Table S1 (Supporting Information). The obtained average lifetimes follow the order of MAI (66 ns) > control (51 ns) > NH_4I (29 ns) > HI (25 ns), indicating that the MAI-based sample has the best film quality likely due to reduced defects.[34] The improved film quality of the MAI-based film may be related to the byproduct CH_3NH_2 gas, which was reported to induce defect-healing of perovskite films.[35]

We investigate the morphologies of the RPP films through scanning electron microscopy (SEM) (**Figure 2**a,b) and tapping-mode atomic force microscopy (AFM) characterizations (Figure 2c). Both the top-view (Figure 2a) and cross-sectional (Figure 2b) SEM images of these films show no obvious difference, showing compact and pinhole-free morphologies, which are highly desirable for efficient devices, especially solar cells The AFM images display wrinkle-patterned surface morphologies with similar values of root-mean-squared (RMS) roughness being 15.7, 18.7, 17.8 and 17.9 nm for the control, HI-, NH_4I-, and MAI-based films, respectively (Figure 2c). We note that the wrinkled morphologies obtained here are quite different from our previous work,[28] because the RPP film was further optimized by annealing in ambient air instead of solvent annealing in glovebox. The formation of wrinkles was proposed to be related to the release of compressive strain during perovskite crystallization.[36,37]

Since we have observed the formation of high-quality RPP films based on our novel strategy, we further investigate the resulting photovoltaic performance employing an inverted planar device configuration as shown in **Figure 3**a. Here poly(3,4-ethylenedioxythiophene):poly(styrenesulfonate) (PEDOT:PSS) and [6,6]-phenyl-C61-butyric acid methylester (PCBM) serve as hole and electron transport layers, respectively. Figure 3b compares current density–voltage (*J–V*) characteristics of our best devices from different precursor solutions, and their detailed photovoltaic parameters are summarized in **Table** 1. Compared to the control device, the HI-based and NH_4I-based devices show slightly lower

efficiency while the MAI-based device presents a higher performance, which correlates well with the observations by XRD and transient PL. Due to the improved film quality, the MAI-based device achieves a best PCE of 14.3% with a high open-circuit voltage (V_{OC}) of 1.22 V, a short-circuit current density (J_{SC}) of 15.2 mA cm^{-2}, and a fill factor (FF) of 76.9%, which is among the highest efficiencies reported for RPP solar cells.[26,38,39] The integrated J_{SC} values calculated from the external quantum efficiency (EQE) spectra (Figure S8a, Supporting Information) are 14.42, 14.22, 13.94, and 14.77 mA cm^{-2} for the control, HI-, NH_4I-, and MAI-based devices, respectively, which are in good agreement with those derived from the *J–V* measurements with discrepancies below 5%. In addition, our devices show negligible photocurrent hysteresis, as evidenced by the overlapping *J–V* curves under different scan rates and scan directions (Figure S8b, Supporting Information). The best MAI-based device shows a steady-state photocurrent of 13.99 mA cm^{-2} under illumination at a constant voltage bias of 1.02 V, generating a stabilized PCE of 14.3% (Figure S8c, Supporting Information).

The statistical distribution of photovoltaic parameters based on 20 devices for each group is presented in Figure S9 and Table S2 in Supporting Information, showing comparable performances between these devices. Average PCEs of 12.9 ± 0.4%, 12.8 ± 0.3%, 12.5 ± 0.3%, and 13.5 ± 0.3% are obtained for the control, HI-, NH_4I-, and MAI-based devices, respectively, showing a similar trend as the performances of the best cells. It is noteworthy that we further optimize the device by annealing in ambient air instead of solvent annealing in glovebox (See the Experimental Section for details), thus the control device showed significantly increased average PCE of 12.9% compared to 10.7% in our previous work.[28] The improved performance can be ascribed to the positive effect of moisture, which was reported to facilitate nucleation and crystallization of the perovskite material, resulting in better film quality.[40,41] The XRD result shows reduced FWHM value from 0.16° (previous work)[28] to 0.10° (this work), confirming the improved film quality. The purchased HI is a water solution, and the addition of HI introduces impurities including a small amount (4.8 vol% vs. DMF) of H_2O, which may be

uncontrollable factors for device performance. In fact, the HI-based precursor solution shows brown color, while the other three precursor solutions are yellow (Figure S10, Supporting Information). Despite similar results for the HI-, NH_4I-, and MAI-based RPP films in our system, NH_4I and MAI prove to be better choices for our method.

Voltage loss (V_{loss}), which is defined as the difference between optical bandgap (E_{gap}) of the active layer and the V_{OC}, is a key parameter that affects the maximum achievable PCE for any type of solar cells.[42] The high V_{OC} of 1.22 V achieved for the MAI-based devices suggests a very low V_{loss} of 0.43 V considering the bandgap of 1.65 eV for the MAI-based RPP film. This motivates us to study V_{loss} in the devices. Highly sensitive Fourier-transform photocurrent spectroscopy-EQE (FTPS-EQE) was conducted to determine the radiative V_{OC} limit ($V_{OC,Rad}$)[43,44], which was calculated to be 1.38 V for a representative MAI-based device (Figure 3c). Physically, $V_{OC,Rad}$ refers to the maximum V_{OC} of the device only considering radiative recombination. The nonradiative recombination V_{OC} loss ($\Delta V_{OC,NR}$) is quantified by measuring the EQE of electroluminescence (EQE_{EL})[45,46]. The MAI-based solar cell exhibits a relatively high EQE_{EL} of 0.13% at a driving current density equal to the J_{SC} (Figure 3d), corresponding to a $\Delta V_{OC,NR}$ value of only 0.17 V based on the equation

$$\Delta V_{OC,NR} = -\frac{kT}{q}\ln(EQE_{EL}) \tag{4}$$

where k is Boltzmann constant, T is temperature, and q is elementary charge. Consequently, the calculated V_{OC} is 1.21 V ($V_{OC,Rad}$ -$\Delta V_{OC,NR}$), which is consistent with the measured V_{OC} (1.22 V). The low value of $\Delta V_{OC,NR}$ is comparable to high-performance 3D perovskite and crystalline silicon solar cells[43,44], indicating suppressed nonradiative recombination and a high-quality RPP film from the MAI-based precursor solution.

We further demonstrate the general applicability of the developed novel strategy on fabricating RPP films with different n values and from different types of RNH_2 for solar cells. We first fabricated $(PEA)_2MA_2Pb_3I_{10}$ (n = 3) and $(PEA)_2MA_5Pb_6I_{19}$ (n = 6) RPP solar cells by

using the $PENH_2$ + MAI method. As shown in Figure S11 in Supporting Information, these devices also show similar performance compared to the control devices with RPP films prepared from purchased PEAI. **Figure 4**a shows the chemical structures of different types of RNH_2. 2-picolylamine ($PCNH_2$), butylamine (BNH_2), 2-phenoxyethylamine ($POENH_2$) and 4-methoxyphenethylamine ($MOPENH_2$) are alkylamines with heterocyclic aromatic, aliphatic, aryl ether and electron-donating aryl building blocks, respectively. To the best of our knowledge, $PCNH_2$, $POENH_2$ and $MOPENH_2$ are used as organic spacers for RPP solar cells for the first time. Several excitonic absorption peaks can be observed in the absorption spectra of the four RNH_2-based RPP films (Figure S12a, Supporting Information), suggesting the formation of mixed RPP phases. The XRD patterns also show strong diffraction signals at $2\theta = 14.1^{o}$ and 28.2^{o} (Figure S12b, Supporting Information), indicating highly preferred orientation. Figure 4b presents the *J-V* curves of these RNH_2-based solar cells, showing decent PCEs of 11.3%, 10.2%, 8.8% and 7.8% for the $PCNH_2$-, BNH_2-, $POENH_2$-, and $MOPENH_2$-based devices, respectively (Table S3, Supporting Information). We have shown previously that the amount of additives (DMSO and MACl) had significant impact on the device performance[28] and here we used the same amount of additives as the PEAI-based device, thus it is expected that further performance improvement for these devices can be achieved by optimization of the additives.

Finally, we extend our method to fabricate RPP LEDs based on $(NMA)_2Cs_{n-1}Pb_nI_{3n+1}$ (NCPI, NMA = 1-naphthylmethylammonium).[27] The HI-, NH_4I-, and MAI-based precursor solutions are prepared using 1-naphthalenemethylamine ($NMNH_2$), which is an alkylamine with a polycyclic aromatic unit (Figure 4a), together with HI, NH_4I and MAI, respectively, to replace NMAI in the control precursor solution. Similarly, the resulting RPP films show no obvious difference by characterizations of absorption, XRD, PL and SEM (Figure S13, Supporting Information), and the RPP LEDs show comparable device performances with a best peak EQE of 6.0% (Figure 4c,d) and electroluminescence (EL) emission peaks at 695 nm (Figure 4e). Here the Cs-based RPP further confirms the reaction paths via Equation 1-3. These

results justify the universality of our method to fabricate high-quality RPP films from different types of RNH_2 for solar cells and LEDs. Furthermore, our method is expected to fabricate green or blue RPP LEDs by replacing I with Br or Cl in the precursor solutions and study new RNH_2-based RPPs for various optoelectronic applications, which are currently under investigation in our group.

In summary, we have developed a straightforward approach to prepare RPP precursor solutions based on commercially available amines (RNH_2) which were supposed to in situ form organic spacer cations (RNH_3^+), avoiding the chemical synthesis processes of RNH_3X. The new precursors enable formation of RPP films with high quality comparable to or even better than the control film. Remarkably, the MAI-based solar cell achieved a best performance with a PCE as high as 14.3%, which is among the highest values for reported RPP solar cells. In addition, an efficient deep red RPP LED has been achieved with a peak EQE of 6.0%, which is among the best red RPP LEDs. In addition, high-quality RPP films have been realized based on different types of RNH_2, indicating the universality of our method. These findings will pave the way to develop new RPPs for various optoelectronic applications.

Experimental Section

Preparation of PEAI films: The PEAI precursor solutions for preparing PEAI films were prepared by dissolving purchased PEAI or $PENH_2$ with equimolar HI, NH_4I and MAI, respectively, in DMF. The PEAI films were deposited by spin-coating the solutions on glass substrates, followed by annealing at 100 °C in N_2–filled glovebox (O_2 and H_2O < 1 ppm).

Preparation of $(PEA)_2PbI_4$ (n = 1) and $(PEA)_2MAPb_2I_7$ (n = 2) films: The control PEAI-based precursor solutions were prepared by dissolving PbI_2, MAI and PEAI in DMF according to their stoichiometric ratios. For the HI-, NH_4I-, and MAI-based precursor solutions, PEAI in

the control precursor was replaced by equimolar $PENH_2$ together with HI, NH_4I and MAI, respectively, while keeping the other materials the same. RPP films were fabricated by directly spin coating the RPP precursor solutions on glass substrates at 4000 rpm for 30 s, followed by annealing at 95 °C for 15 min, in N_2 –filled glovebox.

Preparation of larger-n RPP films (n = 3, 4, 6): The control PEAI-based $(PEA)_2(MA)_3Pb_4I_{13}$ precursor solution was prepared by dissolving PbI_2 (0.95 mmol), $PbCl_2$ (0.05 mmol), MAI (0.85 mmol) and PEAI (0.5 mmol) in mixed solvents of DMF (0.938 mL) and DMSO (0.062 mL) as described in our previous publication[28]. For the HI-, NH_4I-, and MAI-based precursor solutions, PEAI in the control precursor was replaced by equimolar $PENH_2$ together with HI, NH_4I and MAI, respectively, while keeping the other materials the same. To get accurate amount of $PENH_2$, it is suggested to use electronic balance to measure the mass instead of pipetting gun to measure the volume. The precursor solutions were stirred at room temperature for several hours before use. RPP films were fabricated by directly spin coating the RPP precursor solutions onto the substrates at 4000 rpm for 30 s, followed by annealing at 95 °C for 15 min. All the RPP films were annealed in ambient air with humidity of 40 ± 10% unless otherwise specified. The RPP films with n = 3 and 6 were prepared following the same procedures as the n = 4 RPPs. The RPP films with various organic spacer cations were prepared by replacing $PENH_2$ with RNH_2 in the $(PEA)_2(MA)_3Pb_4I_{13}$ films.

Solar cell fabrication. Indium tin oxide (ITO) coated glass substrates were cleaned as routine.[28] PEDOT:PSS (Baytron P-VP AI4083) was spin-coated onto the ITO substrates at 4000 rpm, followed by drying at 140 °C for 10 min in air. Then the samples were transferred into N_2–filled glovebox. RPP films were fabricated following the procedures described above. PCBM was then coated onto the RPP layer at 1000 rpm for 30 s from a chlorobenzene solution (20 mg mL^{-1}). Then, BCP solution with concentration of 0.5 mg mL^{-1} in absolute ethanol was spin-coated without additional annealing. Finally, devices were finished by thermal deposition

of Ag electrode under high vacuum. The active device area was defined as 0.0725 cm^2 by the overlapping of Ag and ITO electrode.

Characterization. A scanning electron microscope (SEM, Philips XL30 FEG SEM) and a tapping-mode atomic force microscope (AFM, Park XE7) were used to characterize the morphology of samples. X-ray diffraction (XRD) measurements were performed with an X'Pert PRO X-ray diffractometer using Cu Kα radiation. Absorption spectra were measured with a PerkinElmer model Lambda 900. External quantum efficiencies (EQEs) of the devices were obtained using an EQE system (QE-R3011, Enli Technology Co. Ltd), and the system was calibrated using a standard crystalline silicon solar cell before measurement. Current density−voltage ($J-V$) characteristics of the devices were measured by using a Keithley 2400 source meter under AM1.5G illumination with intensity of 100 mW cm^{-2}. The light intensity was calibrated by a standard Si solar cell. The voltage was swept from -0.3 V to 1.4 V, then back to -0.2 V with a rate of 52 mV s^{-1} at a step of 20 mV. Transient PL measurements were performed using 400 nm femtosecond excitation pulses (50 fs). The laser pulses were generated by passing the strong fundamental 800 nm femtosecond laser beam (Coherent Libra™, 50 fs) through a beta barium borate (BBO) crystal (frequency doubler). The emitted light was collected at a backscattering angle by an Optronis Optoscope™ streak camera system which has an ultimate temporal resolution of 10 ps.

Supporting Information

Supporting Information is available from the Wiley Online Library or from the author.

Acknowledgements

This work was financially supported by the ERC Starting Grant (717026), National Natural Science Foundation of China (51472164 and 61704077), the 1000 Talents Program for Young Scientists of China, Shenzhen Peacock Plan (KQTD2016053112042971), the Educational Commission of Guangdong Province (2015KGJHZ006 and 2016KCXTD006), the Science and Technology Planning Project of Guangdong Province (2016B050501005), Natural Science Foundation of SZU (000050), the Joint NTU-LiU PhD programme on Materials- and Nanoscience, the European Commission Marie Skłodowska-Curie Actions (691210), and the Swedish Government Strategic Research Area in Materials Science on Functional Materials at Linköping University (Faculty Grant SFO-Mat-LiU no. 2009-00971). X.K.L. is a Marie

Skłodowska-Curie Fellow (798861). T.C.S. and M.L. acknowledge the financial support from JSPS-NTU Joint Research Project M4082176; the Ministry of Education Tier 2 grant MOE 2017-T2-2-002; and from the Singapore National Research Foundation (Programs NRF-CRP14-2014-03, and NRF-NRFI-2018-04).

Received: ((will be filled in by the editorial staff))
Revised: ((will be filled in by the editorial staff))
Published online: ((will be filled in by the editorial staff))

Conflict of Interest

The authors declare no conflict of interest.

References

[1] H. J. Snaith, *Nat. Mater.* **2018**, *17*, 372.

[2] G. Xing, N. Mathews, S. Sun, S. S. Lim, Y. M. Lam, M. Grätzel, S. Mhaisalkar, T. C. Sum, *Science* **2013**, *342*, 344.

[3] M. A. Green, A. Ho-Baillie, H. J. Snaith, *Nat. Photon.* **2014**, *8*, 506.

[4] J. Qing, H.-T. Chandran, Y.-H. Cheng, X.-K. Liu, H.-W. Li, S.-W. Tsang, M.-F. Lo, C.-S. Lee, *ACS Appl. Mater. Interfaces* **2015**, *7*, 23110.

[5] L. N. Quan, F. P. García de Arquer, R. P. Sabatini, E. H. Sargent, *Adv. Mater.* **2018**, 1801996.

[6] *National Renewable Energy Laboratory (NREL).* **2019**, https://www.nrel.gov/pv/cell-efficiency.html.

[7] Y. Cao, N. Wang, H. Tian, J. Guo, Y. Wei, H. Chen, Y. Miao, W. Zou, K. Pan, Y. He, H. Cao, Y. Ke, M. Xu, Y. Wang, M. Yang, K. Du, Z. Fu, D. Kong, D. Dai, Y. Jin, G. Li, H. Li, Q. Peng, J. Wang, W. Huang, *Nature* **2018**, *562*, 249.

[8] K. Lin, J. Xing, L. N. Quan, F. P. G. de Arquer, X. Gong, J. Lu, L. Xie, W. Zhao, D. Zhang, C. Yan, W. Li, X. Liu, Y. Lu, J. Kirman, E. H. Sargent, Q. Xiong, Z. Wei, *Nature* **2018**, *562*, 245.

[9] T. Leijtens, G. E. Eperon, N. K. Noel, S. N. Habisreutinger, A. Petrozza, H. J. Snaith,

Adv. Energy Mater. **2015**, *5*, 1500963.

[10] T. A. Berhe, W.-N. Su, C.-H. Chen, C.-J. Pan, J.-H. Cheng, H.-M. Chen, M.-C. Tsai, L.-Y. Chen, A. A. Dubale, B.-J. Hwang, *Energy Environ. Sci.* **2016**, *9*, 323.

[11] X.-K. Liu, F. Gao, *J. Phys. Chem. Lett.* **2018**, *9*, 2251.

[12] Y. Chen, Y. Sun, J. Peng, J. Tang, K. Zheng, Z. Liang, *Adv. Mater.* **2017**, 1703487.

[13] S. Ma, M. Cai, T. Cheng, X. Ding, X. Shi, A. Alsaedi, T. Hayat, Y. Ding, Z. a. Tan, S. Dai, *Sci. China Mater.* **2018**, *61*, 1257.

[14] L. N. Quan, M. Yuan, R. Comin, O. Voznyy, E. M. Beauregard, S. Hoogland, A. Buin, A. R. Kirmani, K. Zhao, A. Amassian, D. H. Kim, E. H. Sargent, *J. Am. Chem. Soc.* **2016**, *138*, 2649.

[15] N. Wang, L. Cheng, R. Ge, S. Zhang, Y. Miao, W. Zou, C. Yi, Y. Sun, Y. Cao, R. Yang, Y. Wei, Q. Guo, Y. Ke, M. Yu, Y. Jin, Y. Liu, Q. Ding, D. Di, L. Yang, G. Xing, H. Tian, C. Jin, F. Gao, R. H. Friend, J. Wang, W. Huang, *Nat. Photon.* **2016**, *10*, 699.

[16] M. Ban, Y. Zou, J. P. Rivett, Y. Yang, T. H. Thomas, Y. Tan, T. Song, X. Gao, D. Credington, F. Deschler, H. Sirringhaus, B. Sun, *Nat. Commun.* **2018**, *9*, 3892.

[17] Z. Chen, Y. Guo, E. Wertz, J. Shi, *Adv. Mater.* **2018**, 1803514.

[18] R. Yang, R. Li, Y. Cao, Y. Wei, Y. Miao, W. L. Tan, X. Jiao, H. Chen, L. Zhang, Q. Chen, H. Zhang, W. Zou, Y. Wang, M. Yang, C. Yi, N. Wang, F. Gao, C. R. McNeill, T. Qin, J. Wang, W. Huang, *Adv. Mater.* **2018**, 1804771.

[19] L. Gan, J. Li, Z. Fang, H. He, Z. Ye, *J. Phys. Chem. Lett.* **2017**, *8*, 5177.

[20] J. V. Passarelli, D. J. Fairfield, N. A. Sather, M. P. Hendricks, H. Sai, C. L. Stern, S. I. Stupp, *J. Am. Chem. Soc.* **2018**, *140*, 7313.

[21] H. Hu, F. Meier, D. Zhao, Y. Abe, Y. Gao, B. Chen, T. Salim, E. E. Chia, X. Qiao, C. Deibel, Y. M. Lam, *Adv. Mater.* **2018**, *30*, 1707621.

[22] J. Hu, L. Yan, W. You, *Adv. Mater.* **2018**, 1802041.

[23] L. Zhao, N. Rolston, K. M. Lee, X. Zhao, M. A. Reyes‐Martinez, N. L. Tran, Y. W.

Yeh, N. Yao, G. D. Scholes, Y. L. Loo, A. Selloni, R. H. Dauskardt, B. P. Rand, *Adv. Funct. Mater.* **2018**, *28*, 1802060.

[24] Z. Xiao, R. A. Kerner, L. Zhao, N. L. Tran, K. M. Lee, T.-W. Koh, G. D. Scholes, B. P. Rand, *Nat. Photon.* **2017**, *11*, 108.

[25] Z. Xiao, D. Wang, Q. Dong, Q. Wang, W. Wei, J. Dai, X. Zeng, J. Huang, *Energy Environ. Sci.* **2016**, *9*, 867.

[26] W. Fu, J. Wang, L. Zuo, K. Gao, F. Liu, D. S. Ginger, A. K. Y. Jen, *ACS Energy Lett.* **2018**, *3*, 2086.

[27] J. Chang, S. Zhang, N. Wang, Y. Sun, Y. Wei, R. Li, C. Yi, J. Wang, W. Huang, *J. Phys. Chem. Lett.* **2018**, *9*, 881.

[28] J. Qing, X.-K. Liu, M. Li, F. Liu, Z. Yuan, E. Tiukalova, Z. Yan, M. Duchamp, S. Chen, Y. Wang, S. Bai, J.-M. Liu, H. J. Snaith, C.-S. Lee, T. C. Sum, F. Gao, *Adv. Energy Mater.* **2018**, *8*, 1800185.

[29] J. I. Brauman, J. M. Riveros, L. K. Blair, *J. Am. Chem. Soc.* **1971**, *93*, 3914.

[30] J. Graton, C. Laurence, M. Berthelot, J.-Y. Le Questel, F. Besseau, E. D. Raczynska, *J. Chem. Soc., Perkin Trans. 2* **1999**, 997.

[31] D. Zhao, Y. Yu, C. Wang, W. Liao, N. Shrestha, C. R. Grice, A. J. Cimaroli, L. Guan, R. J. Ellingson, K. Zhu, *Nat. Energy* **2017**, *2*, 17018.

[32] Y. Liao, H. Liu, W. Zhou, D. Yang, Y. Shang, Z. Shi, B. Li, X. Jiang, L. Zhang, L. N. Quan, R. Quintero-Bermudez, B. R. Sutherland, Q. Mi, E. H. Sargent, Z. Ning, *J. Am. Chem. Soc.* **2017**, *139*, 6693.

[33] J. Liu, J. Leng, K. Wu, J. Zhang, S. Jin, *J. Am. Chem. Soc.* **2017**, *139*, 1432.

[34] F. Wang, W. Geng, Y. Zhou, H. H. Fang, C. J. Tong, M. A. Loi, L. M. Liu, N. Zhao, *Adv. Mater.* **2016**, *28*, 9986.

[35] Z. Zhou, Z. Wang, Y. Zhou, S. Pang, D. Wang, H. Xu, Z. Liu, N. P. Padture, G. Cui, *Angew. Chem. Int. Ed.* **2015**, *54*, 9705.

[36] K. Sveinbjörnsson, K. Aitola, J. Zhang, M. B. Johansson, X. Zhang, J.-P. Correa-Baena, A. Hagfeldt, G. Boschloo, E. M. Johansson, *J. Mater. Chem. A* **2016**, *4*, 16536.

[37] S. Braunger, L. E. Mundt, C. M. Wolff, M. Mews, C. Rehermann, M. Jošt, A. Tejada, D. Eisenhauer, C. Becker, J. A. Guerra, E. Unger, L. Korte, D. Neher, M. C. Schubert, B. Rech, S. Albrecht, *J. Phys. Chem. C* **2018**, *122*, 17123.

[38] X. Zhang, X. Ren, B. Liu, R. Munir, X. Zhu, D. Yang, J. Li, Y. Liu, D.-M. Smilgies, R. Li, Z. Yang, T. Niu, X. Wang, A. Amassian, K. Zhao, S. F. Liu, *Energy Environ. Sci.* **2017**, *10*, 2095.

[39] H. Lai, B. Kan, T. Liu, N. Zheng, Z. Xie, T. Zhou, X. Wan, X. Zhang, Y. Liu, Y. Chen, *J. Am. Chem. Soc.* **2018**, *140*, 11639.

[40] J. You, Y. M. Yang, Z. Hong, T.-B. Song, L. Meng, Y. Liu, C. Jiang, H. Zhou, W.-H. Chang, G. Li, Y. Yang, *Appl. Phys. Lett.* **2014**, *105*, 183902.

[41] C.-H. Chiang, M. K. Nazeeruddin, M. Grätzel, C.-G. Wu, *Energy Environ. Sci.* **2017**, *10*, 808.

[42] S. Chen, Y. Wang, L. Zhang, J. Zhao, Y. Chen, D. Zhu, H. Yao, G. Zhang, W. Ma, R. H. Friend, P. C. Y. Chow, F. Gao, H. Yan, *Adv. Mater.* **2018**, *30*, 1804215.

[43] D. Bi, W. Tress, M. I. Dar, P. Gao, J. Luo, C. Renevier, K. Schenk, A. Abate, F. Giordano, J.-P. C. Baena, J.-D. Decoppet, S. M. Zakeeruddin, M. K. Nazeeruddin, M. Grätzel, A. Hagfeldt, *Sci. Adv.* **2016**, *2*, e1501170.

[44] X. Liu, X. Du, J. Wang, C. Duan, X. Tang, T. Heumueller, G. Liu, Y. Li, Z. Wang, J. Wang, F. Liu, N. Li, C. J. Brabec, F. Huang, Y. Cao, *Adv. Energy Mater.* **2018**, 1801699.

[45] J. Yao, T. Kirchartz, M. S. Vezie, M. A. Faist, W. Gong, Z. He, H. Wu, J. Troughton, T. Watson, D. Bryant, J. Nelson, *Phys. Rev. Appl.* **2015**, *4*, 014020.

[46] W. Fu, J. Wang, L. Zuo, K. Gao, F. Liu, D. S. Ginger, A. K.-Y. Jen, *ACS Energy Lett.* **2018**, *3*, 2086.

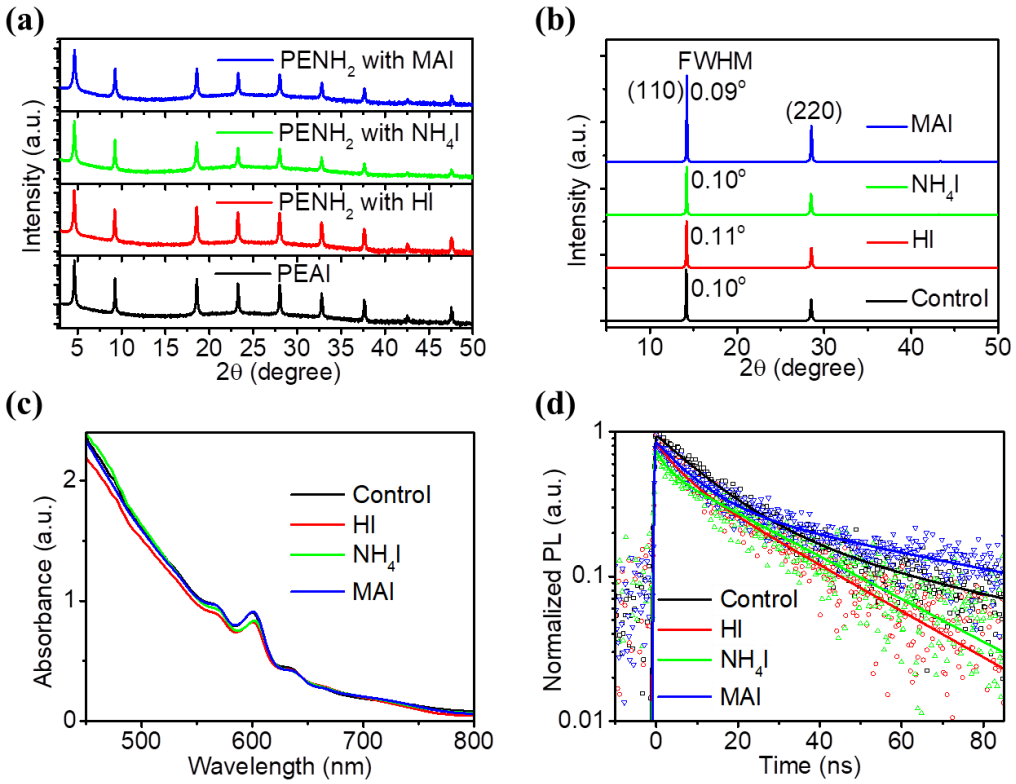

Figure 1. a) XRD patterns for purchased PEAI and films obtained from solutions of $PENH_2$ with HI, NH_4I or MAI. b) XRD patterns, c) UV–vis absorption spectra and d) transient PL decay curves of the RPP films from different precursor solutions.

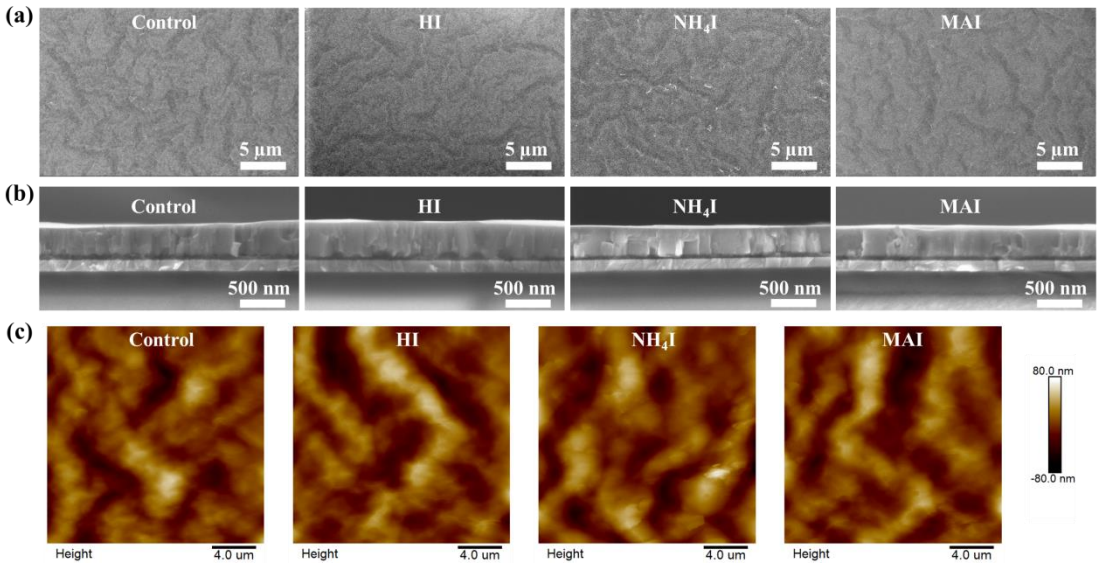

Figure 2. a) Top-view SEM images, b) cross-sectional SEM images and c) AFM images of the RPP films from different precursor solutions. The films are deposited on ITO/PEDOT:PSS substrates.

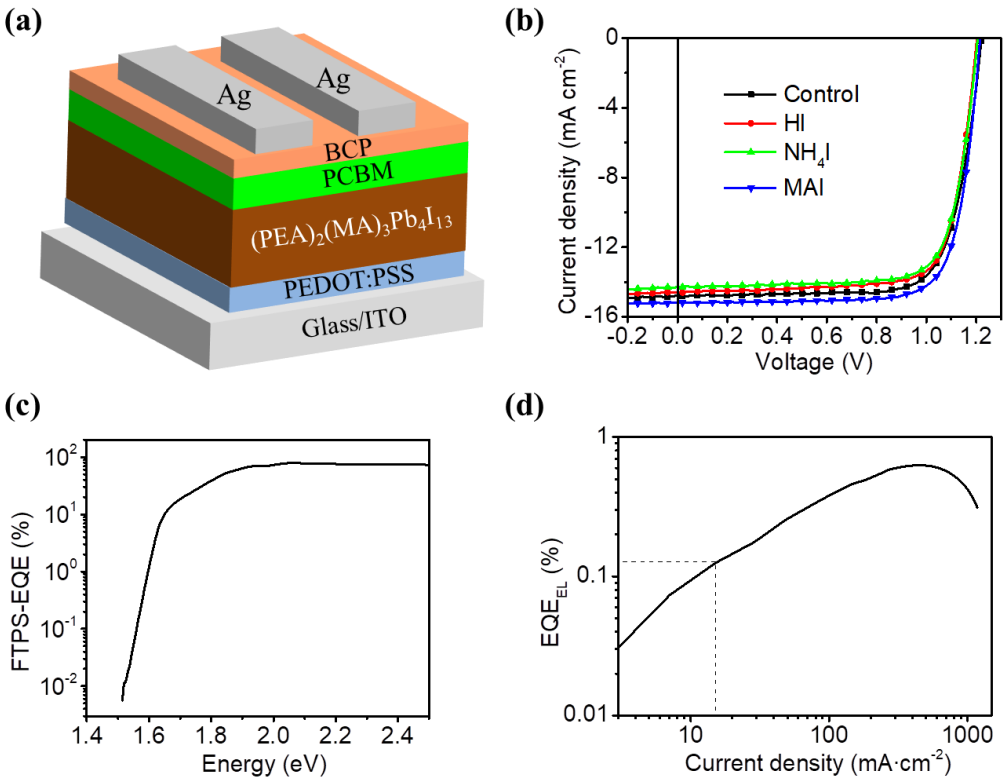

Figure 3. a) A schematic of the device structure. b) *J–V* curves of the champion devices from different precursor solutions. c) FTPS-EQE and d) EQE_{EL} of a representative MAI-based solar cell.

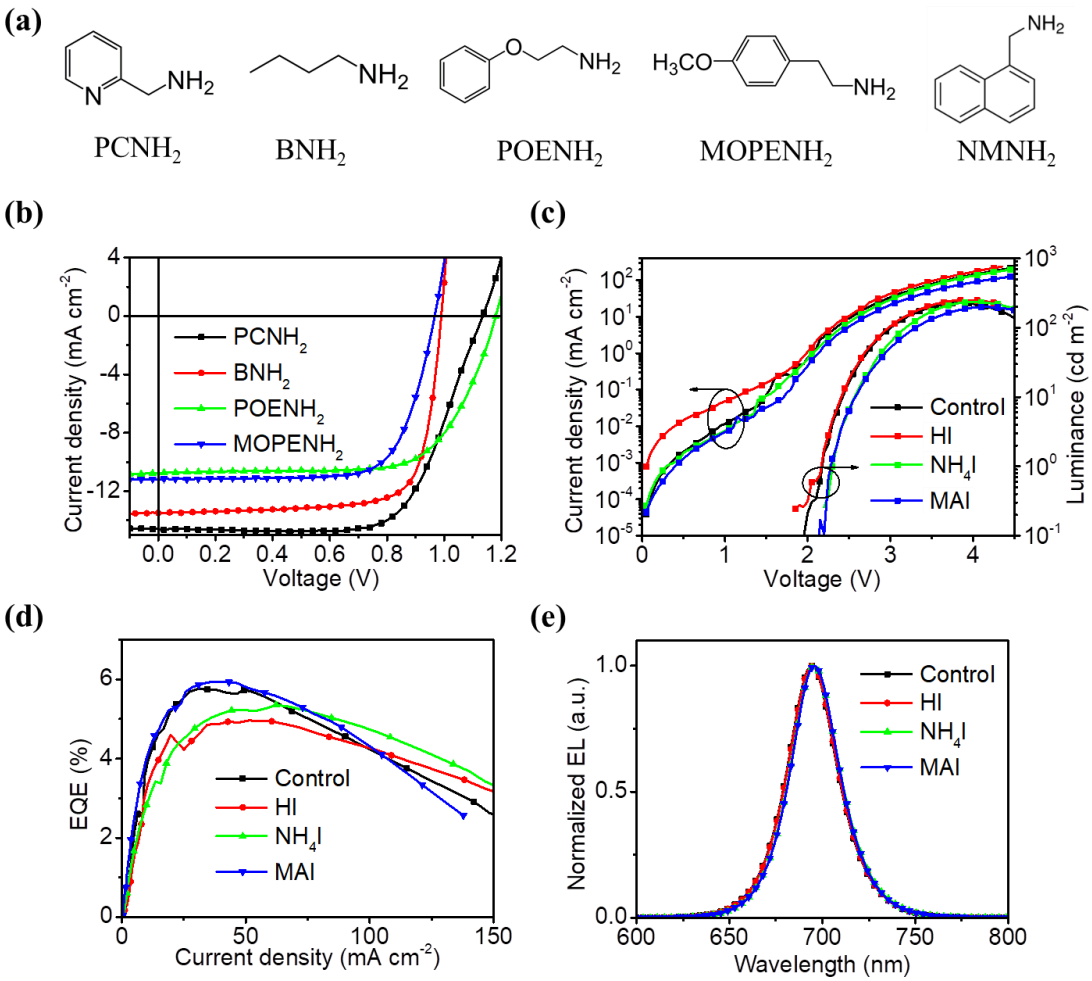

Figure 4. a) Chemical structures of $PCNH_2$, BNH_2, $POENH_2$, $MOPENH_2$ and $NMNH_2$. b) *J*–*V* curves of the four RNH_2-based RPP solar cells. c) Current density–voltage–luminance curves and d) EQE versus current density of RPP LEDs from different precursor solutions. e) Normalized EL spectra of the LEDs under 3.5 V.

Table 1. Photovoltaic parameters of the best performing devices from different precursor solutions.

Devices	V_{OC} (V)	J_{SC} (mA cm^{-2})	FF (%)	PCE (%)
Control	1.22	14.8	75.5	13.6
HI	1.20	14.6	76.4	13.4
NH_4I	1.20	14.3	76.5	13.1
MAI	1.22	15.2	76.9	14.3